Journal of Cleaner Production 172 (2018) 2919–2930

Contents lists available at ScienceDirect

Journal of Cleaner Production

journal homepage: www.elsevier.com/locate/jclepro

Photoremediation of toxic dye from aqueous environment using monometallic and bimetallic quantum dots based nanocomposites

Gaurav Sharma [a, b, c], Anuj Kumar [c], Mu Naushad [d, *], Amit Kumar [a, b, c],
Ala'a H. Al-Muhtaseb [e], Pooja Dhiman [f], Ayman A. Ghfar [d], Florian J. Stadler [a], M.R. Khan [d]

[a] College of Materials Science and Engineering, Shenzhen Key Laboratory of Polymer Science and Technology, Guangdong Research Center for Interfacial Engineering of Functional Materials, Nanshan District Key Lab for Biopolymers and Safety Evaluation, Shenzhen University, Shenzhen, 518060, PR China
[b] Key Laboratory of Optoelectronic Devices and Systems of Ministry of Education and Guangdong Province, College of Optoelectronic Engineering, Shenzhen University, Shenzhen, 518060, PR China
[c] School of Chemistry, Shoolini University, Solan, 173212, Himachal Pradesh, India
[d] Department of Chemistry, College of Science, Building #5, King Saud University, Riyadh, 11451, Saudi Arabia
[e] Department of Petroleum and Chemical Engineering, College of Engineering, Sultan Qaboos University, Muscat, Oman
[f] Department of Physics, IEC University, Baddi, Himachal Pradesh, India

ARTICLE INFO

Article history:
Received 12 June 2017
Received in revised form
15 November 2017
Accepted 16 November 2017
Available online 20 November 2017

Keywords:
Monometallic
Bimetallic
Nanocomposite
Quantum dots
Photocatalyst
Dye

ABSTRACT

Iron nanoparticles (Fe NPs), monometallic Fe@carbon quantum dots (Fe@CQDs) and bimetallic Fe/Ag@carbon quantum dots (Fe/Ag@CQDs) nanocomposites were prepared by simple co-precipitation/reduction method. The nanoparticles (NPs), monometallic nanocomposite (MNCs) and bimetallic nanocomposite (BMNCs) were characterized using various techniques. The adsorptional/photocatalytic activity of NPs, MNCs, and BMNCs were investigated for the removal of fast green (FG) dye from aqueous medium. The degradation of FG dye under combined adsorptional/photocatalytic condition was efficient. The catalytic nature of synthesized NPs, MNCs and BMNCs was also explored for the oxidation of benzyl alcohol and esterification of acetic acid. For oxidation of benzyl alcohol with H_2O_2 in the presence of acetonitrile (ratio of butyl alcohol: H_2O_2 was 2:1) at temperature 80 °C, the Fe NPs gave maximum yield (87%). The esterification of acetic acid with ethyl, isopropyl and butyl alcohol showed that butyl alcohol gave maximum yield of 82%, 80%, and 84% for Fe NPs, Fe@CQDs MNCs and Fe/Ag@CQDs BMNCs, respectively.

1. Introduction

Dye-contaminated wastewater from the industries contributes drastically to copious diseases, such as hypertension, hemolysis, organ damage, respiratory disorders in humans and aquatic animals (Sharma et al., 2016c). Moreover, various contaminants for instance, natural organic matters, microorganisms and heavy metals further deteriorate this problem (Mittal et al., 2016; Naushad et al., 2015). The removal of these organic pollutants from water system is a priority for ensuring a safe and clean environment (Al-Ghouti et al., 2003; Galán et al., 2013). Dyes are mostly categorized as anionic (acidic), cationic (basic) and nonionic. Fast Green dye is cationic dye which is used as a quantitative stain for histones in alkaline medium. Several methods have been used for the removals of dyes such as membrane separation, coagulation, reverse osmosis, chemical oxidation and aerobic & anaerobic microbial degradation. One of the most important methods so far is adsorption, because of its ease, efficiency and economy(Sharma et al., 2017c). Though, to fight tenacious pollutants in bodies of water, numerous other new methods have been used as an alternative to adsorption such as adsorptional/photocatalytic process (Kumar et al., 2017a). The emerging field of nanoparticle science is giving scientists and engineers' new possibilities in environmental detoxification research. A wide variety of physical, chemical, and biological processes are used to produce nanoparticles with sizes between 1 and 100 nm (Yu et al., 2009). Thus, nanoparticles may be defined as small objects behaving as an entire unit in terms of their transport and chemical properties. Nanoparticles have gained vast importance due to their small size (but large surface area), physical properties and their presences also increase the importance or

---

* Corresponding author.
E-mail address: mnaushad@ksu.edu.sa (M. Naushad).

https://doi.org/10.1016/j.jclepro.2017.11.122
0959-6526/

value of other materials, with which they are blended (Sharma et al., 2017b). Nanoparticles research is presently an area of extreme scientific importance, due to their wide-range of potential applications in biomedical, optical and electronic fields (Sharma et al., 2015). At present, mono and bimetallic nanoparticles of many pure metals have been fabricated (Akhundi and Habibi-Yangjeh, 2015; Omidi et al., 2013; Poormohammadi-Ahandani and Habibi-Yangjeh, 2010). In bio-applications, nanoparticles of non-toxic metals, particularly silver and gold have been much investigated (Tang et al., 2013; Zhang et al., 2017). Due to cost effective nature and non-toxic behavior, the iron is another potential candidate for nanoparticles synthesis. However, as iron is highly reactive metal, the synthesis of iron-based nanoparticles is a tedious process. Iron-based nanoparticles found various applications in the fields such as sensors, environment remediation, biomedical engineering etc, (Fu and Ravindra, 2012; Martinez-Cabanas et al., 2016; Sharma et al., 2016a).

Metallic nanoparticles have been classified as monometallic, bimetallic and trimetallic. These three groups have received considerable attention in recent years because of their tailorable chemical and physical properties. The bimetallic nanoparticles display new physicochemical properties, when the spatial distribution of the metals are inhomogeneous, i.e. if the second metal is preferentially located on the first metal surface or its interior upon formation of bimetallic nanoparticles (BMNPs), which are neither observed in individual molecules nor in bulk metals (Sharma et al., 2017). For example, silver-based bimetallic nanoparticles display strong absorption of electromagnetic wave in the visible range due to surface plasmon resonance, turning such silver nanoparticle suspensions yellow (Gorham et al., 2012). Bimetallic nanoparticles are unstable, thus undergo fast oxidation and easily aggregate in a solution, which inhibits their applications in sensors and optical instruments. They also have an extensive range of applications in microelectronics, optical devices, catalysis, drug delivery systems etc, (Yang et al., 2014). Metallic silver forms good compactable component in bimetallic nanoparticles, as silver astonishingly shows light absorbing and scattering properties and, unlike many dyes and pigments, its color depends on the size and the shape of its particles. Silver-based nanoparticles are used in various technologies and merged into a wide range of consumer products which take benefit of their appropriate optical, conductive and antibacterial properties (Rai et al., 2012). The BMNPs show higher catalytic selectivity and activity than MNPs. Addition of one more extra metal into the system increases the performance of BMNPs, enabling their more applications in different fields. In recent times, composites of nanoparticles have attracted more attention because of their better properties like large surface area, chemical and thermal stabilities, improvement in the mechanical performance etc, (Sharma et al., 2016b). A very special feature of magnetic nanoparticles is that their magnetic properties can be utilized in separation processes and sensing. Due to the rich physiochemical properties of these NPs they can furthermore, be used as catalyst in many organic reactions (Gupta and Gupta, 2005; Kumar et al., 2015). Thus, nanoparticles and their nanocomposite are promising materials with board range of applications(Naushad et al., 2016; Pathania et al., 2016a).

In the present paper, we have worked on the fabrication and application of Fe NPs, Fe@CQDs MNCs and Fe/Ag@CQDs BMNCs. The photodegradation of FG dye using indigenously synthesized NPs, MNCs and BMNCs was investigated. We have also focused on the study of catalytic activity of NPs, MNCs, and BMNCs for organic reaction as oxidation and esterification.

2. Materials and methods

2.1. Chemicals and reagents

In this study, the chemicals used were of analytical reagent grade. Sodium borohydride, ferric chloride, ethanol, butanol, silver nitrate and isopropyl alcohol were obtained from Loba Chemie Pvt., Ltd., India. D-fructose and FG dye were obtained from CDH Pvt. Ltd., India. Sodium hydroxide obtained from RANKEM, Avantor, Performance Material India, Ltd.

2.2. Synthesis of Fe NPs

In a two necked round-bottom flask, 50 mL (3.5 mM) aqueous solution of ferric chloride was freshly prepared in double distilled water with constant stirring for 30 min. In another beaker, 50 mL (32 mM) aqueous solution of sodium borohydride was prepared. The solution of sodium borohydride was added drop wise to the freshly prepared ferric chloride solution under constant stirring. Black precipitates of Fe were formed alongside vigorous gas production (H_2) which continued for 15–20 min. The resulting black precipitates were further aged by keeping them in solution for another 1 h to complete the reaction. Use of large excess of sodium borohydride is the key factor for the fast and uniform growth of iron particles. These iron particles were washed with large volume of water several times, until a clear filtrate was obtained (Herranz et al., 2014; Martínez-Mera et al., 2007; Sun and Zeng, 2002).

2.3. Synthesis of carbon quantum dots

The carbon quantum dots (CQDs) aqueous solution was prepared by mixing 5 mL of D-fructose (500 mM) and 5 mL of NaOH (500 mM) (Bozetine et al., 2016). The resultant mixture solution was heated at 60 W for 15 min in microwave oven to obtain carbon quantum dots.

2.4. Synthesis of Fe@CQDs MNCs and Fe/Ag@CQDs BMNCs

The Fe@CQDs MNCs and Fe/Ag@CQDs BMNCs were synthesized by co-precipitation/reduction method. For synthesis of Fe@CQDs, to the above synthesized carbon quantum dots solution, 50 mL of freshly prepared ferric chloride (3.5 mM) solution was added. Afterward, 50 mL of sodium borohydride (32 mM) solution was added dropwise under continuous stirring. The resulting solution was vigorously stirred for 30 min at 60 °C. The resultant black precipitates were further aged by keeping them in the solution for 1 h, resulting in a slight change in precipitates color from black to brownish-black. The obtained precipitates were filtered, washed and dried at 50 °C in a forced convection oven.

For the synthesis of Fe/Ag@CQDs BMNCs to the above-described synthesized carbon dots solution, freshly prepared 50 mL of ferric chloride (3.5 mM) and 50 mL of silver nitrate (3.5 mM) solutions were mixed. Afterward, 50 mL of sodium borohydride (32 mM) solution was added drop wise under constant stirring. Grayish black color precipitates were formed along with a vigorous gas production. Then, the resultant mixture was stirred for 2 h. The obtained precipitates were filtered, washed and dried at 50 °C in a forced convection oven. The obtained Fe@CQDs and Fe/Ag@CQDs particles were stored for further studies.

2.5. Characterization

The FTIR (Fourier-transform infrared spectroscopy) spectra of Fe NPs, Fe@CQDs MNCs, and Fe@CQDs BMNCs were obtained by Perkin ElmerSpectrum-BX USA in the range of 400–4000 cm^{-1}. The X-ray diffraction data was recorded using an X-ray diffractrometer (XPERT-PROX-ray) and diffraction pattern of the materials were obtained using CuK$_\alpha$ radiation ($\lambda = 1.5418$ Å). The physical properties such as morphology and shape were studied by scanning electron microscopy (Quanta 250, FEI Make Mode No. D9393). Transmission electron microscopy was used for obtaining the particles size of MNCs and BMNCs. The particle size of Fe@CQDs MNCs and Fe@CQDs BMNCs were found by dissolving the prepared samples in ethanol and analyzed under (Techni G2 20 S-Twin) transmission electron microscopy using an acceleration voltage of 200 kV. The nature of the optical band gap was found using the fundamental absorption, which corresponds to electron excitation from valence band to conduction band. Direct absorption band gaps of the Fe NPs, Fe@CQDs MNCs and Fe/Ag@CQDs BMNCs were obtained by confirming the absorption data to Tauc equation.

$$\alpha h\nu = B(h\nu - E_g)^n \tag{1}$$

The optical band gap was evaluated by extrapolating the straight portion of the curve between $(\alpha h\nu)^2$ and hν when $\alpha = 0$.

Vibrating sample magnatometry (Microsense"EV7, USA) study was used to presents the ferromagnetic state of the Fe@CQDs MNCs and Fe@CQDs BMNCs.

2.6. Applications

2.6.1. Photodegradation of fast green dye

Synthesized NPs, MNCs, and BMNCs were studied for their photocatalytic behavior against fast green dye. The photocatalytic experiments were performed using a double walled glass chamber photo-reactor covered with thermostat to maintain constant temperature. 100 mg of synthesized NPs, MNCs and BMNCs were added into solution of fast green (1×10^{-5} mol L^{-1}) dye. The two sets of fast green dye slurries were made for each NPs, MNCs and BMNCs. In the first condition, the sets were kept under dark to attain the adsorption/desorption equilibrium and in the second condition, the test sets were placed directly in sodium light for combined adsorptional/photocatalysis (Pathania et al., 2016b; Sharma et al., 2017a, 2016c; Zhang et al., 2014). Once the equilibrium was established under first sets of condition, the solutions were further exposed to sodium light with intermittent agitation for photocatalysis (adsorption in dark followed by photocatalysis). A aliquot of 3 mL was taken out at numerous intervals of time and centrifuged to eliminate any solid NPs, MNCs, or BMNCs particles. Absorbance was measured between 200 and 750 nm(Kumar et al., 2017b). The photocatalysis degradation of fast green dye was investigated at 620 nm. The degradation percentage was calculated by the following equation:

$$degradation = \frac{A_0 - A}{A_0} \times 100\% \tag{2}$$

where, A_0 is the initial absorbance of dye, A is the absorbance of dye after time t (min.).

2.6.2. Exploring catalytic nature of synthesized NPs, MNCs and BMNCs for organic reactions

For the oxidation reaction procedure, benzyl alcohol and hydrogen peroxide were taken in volume ratio of 2:1. To the above reaction mixture, 1 mL acetonitrile was added as solvent. The reaction mixture was refluxed for 2 h at different temperatures (i.e., 80 °C and 100 °C) using NPs, MNCs, and BMNCs as catalysts. For comparison, the reaction was also performed without acetonitrile and catalyst. For the esterification reaction procedure, acetic acid and various alcohols were taken in the ratio of 2:1 directly into the round bottom flask along with NPs, MNCs and BMNCs as catalysts. 10–15 mL of a suitable solvent such as toluene or cyclohexane was added to these reaction mixtures. Reaction mixture was refluxed for 2.5 h at 110 °C. The reaction yield was calculated using formula as follows:

$$\%yield = \frac{W_r - W_p}{W_r} X\ 100 \tag{3}$$

where, W_r is the initial weight of the reactants and W_P is the weight of products formed.

3. Results and discussion

3.1. Characterization

The Fe NPs, Fe@CQDs MNCs and Fe/Ag@CQDs BMNCs were synthesized using Co-precipitation/reduction method. Fig. 1 (a) shows the Fourier transform infrared spectrum of the Fe NPs. The peaks at 579 cm^{-1} and 3247 cm^{-1} corresponds to the Fe–O and O–H stretching frequencies. The peak at 1614 cm^{-1} corresponds to the H-O-H stretching frequency. This confirmed the successful

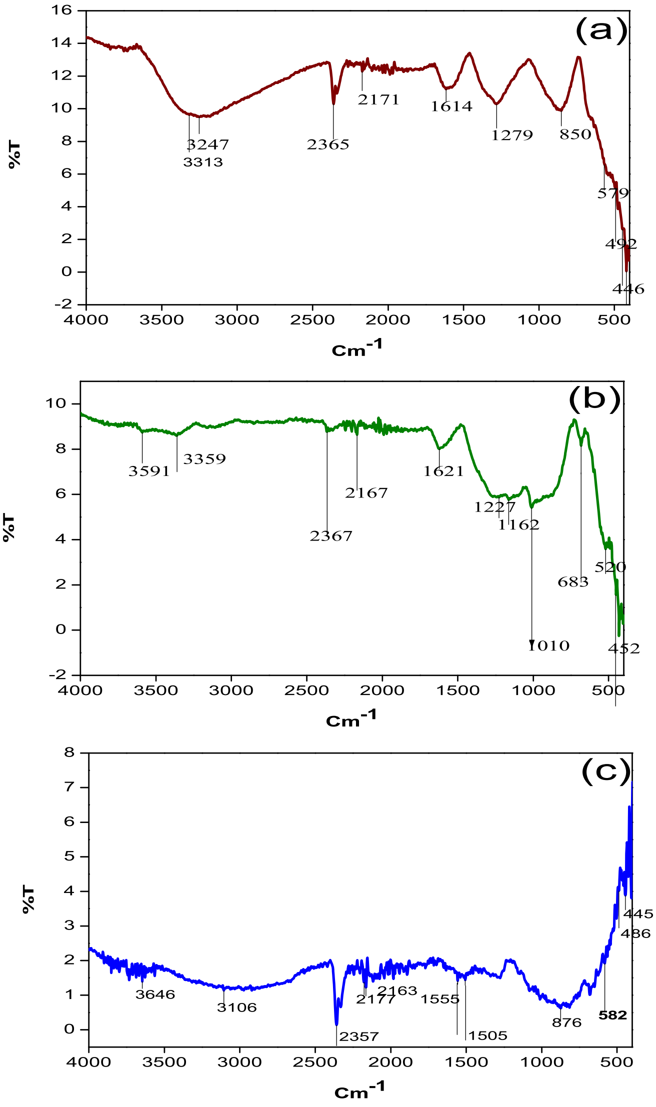

Fig. 1. FTIR spectrum of (a) Fe NPs, (b) Fe@CQDs MNCs and (c) Fe/Ag@CQDs BMNCs.

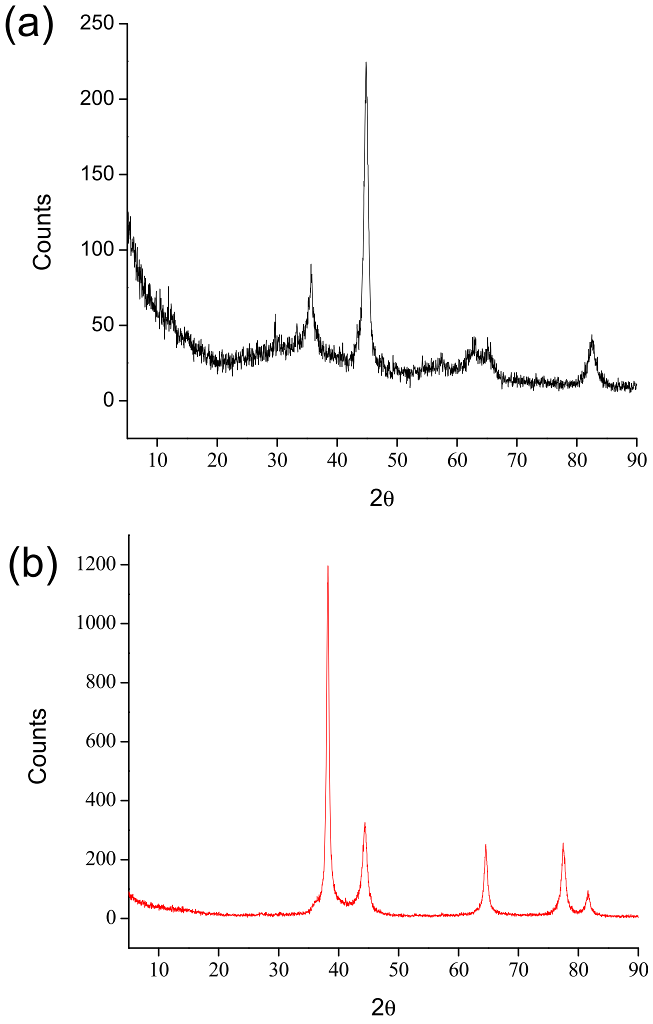

Fig. 2. XRD patterns of (a) Fe@CQDs MNCs and (b) Fe/Ag@CQDs BMNCs.

formation of Fe NPs. Fig. 1 (b) shows the FTIR spectrum of the Fe@CQDs MNCs. The spectrum had a broad peak of O-H stretching vibration mode at 3359 cm^{-1} due to the CQDs. The peak for Fe-O shifted to 520 cm^{-1}, while the same peak was located at 579 cm^{-1} in the spectrum of Fe NPs. The band at 1621 cm^{-1} was assigned to H-O-H stretching frequency, while the peaks at 1162 $cm^{-1}$and 1227 cm^{-1} corresponds to C-O vibrations of oxygen containing groups. This confirmed the successful formation of Fe@CQDs MNCs. The FTIR spectrum of Fe/Ag@CQDs BMNCs (Fig. 1 (c)) shows the peaks at 1660 cm^{-1} and 3307 cm^{-1} which were assigned to C=C stretching and O-H broadening. The shifting of peaks was observed for Fe-O to 486 cm^{-1} in case of Fe/Ag@CQDs BMNCs. Fig. 2 (a) shows the XRD spectra of synthesized Fe@CQDs MNCs and Fe/Ag@CQDs BMNCs. The peaks at 2θ value of 30°, 35°, 45°, 63° and 65° corresponds to the (220), (311), (400), (422) and (440) diffraction planes of the spinel cubic structure of iron particles (Mostafaei and Nasirpouri, 2013; Wang et al., 2015). In Fig. 2 (b) the data showed diffraction peaks at 2θ value of 38°, 44°, 64°, 77° and 81°, which were indexed to (111), (200), (220), (311) and (222) planes of silver. The XRD results showed that there was change in 2θ value of Fe/Ag@CQDs BMNCs as compared to Fe@CQDs MNCs. The additional peaks (Fig. 2b) due to the presence of silver in the Fe/Ag@CQDs BMNCs were also seen. Therefore, the XRD results confirmed the formation of Fe@CQDs MNCs and Fe/Ag@CQDs BMNCs.

The scanning electron micrographs of Fe NPs, Fe@CQDs MNCs and Fe/Ag@CQDs BMNCs were obtained using scanning electron microscope (Figures are given in the supplementary material as S1). Fig. S1 (a,b,c and d) and Fig. S1 (e,f,g and h) shows the SEM images of Fe NPs and Fe@CQDs MNCs at different magnification indicating that Fe NPs are rough, spherical and highly agglomerated. Fig.S1 (e,f,g and h) reveals that upon addition of CQDs for formation of Fe@CQDs MNCs, the surface morphology changed to smooth and is fibrous in nature as compared to Fe NPs. Fig. S1 (i, j, k and l) shows the SEM images of Fe/Ag@CQDs BMNCs. Fig. S1 (i, j, k and l) reveals that the addition of Ag for the fabrication of Fe/Ag@CQDs BMNCs, the surface morphology changed again and became fibrous with irregular texture. The SEM results confirmed the formation of Fe NPs, Fe@CQDs MNCs and Fe/Ag@CQDs BMNCs.

TEM images of Fe@CQDs MNCs and Fe/Ag@CQDs BMNCs were shown in Fig. 3 (a, b and c) and Fig. 3 (d,e and f) at diverse magnification. The TEM images showed that the average size of particles was less than 50 nm for both Fe@CQDs MNCs and Fe/Ag@CQDs BMNCs and high agglomeration can be clearly seen, which may be due to the magnetic nature of synthesized materials.

The nature of the optical band gap was determined using the fundamental absorption, which corresponded to the excitation of electron from valence band to conduction band. Direct absorption band gaps of the Fe NPs, Fe@CQDs MNCs and Fe/Ag@CQDs BMNCs was obtained by confirming the absorption data to the Tauc equation in Fig. 4.

The band gaps of the Fe NPs, Fe@CQDs MNCs and Fe/Ag@CQDs BMNCs were calculated by using Tauc relation. The tauc plots for Fe NPs, Fe@CQDs MNCs and Fe/Ag@CQDs BMNCs were represented in Fig. 4. The band gap for Fe is 2.44eV, which lies in the range of semiconductors (< 4 eV). So it can find applications in spintronics, thermistors, sensors, and other semiconductors devices (Millo et al., 2001; He and Qi, 2002). The band gap of Fe@CQDs MNCs is 2.39 eV and Fe/Ag@CQDs BMNCs is 1.9 eV. The band gap of Fe/Ag@CQDs BMNCs is lower than the of Fe NPs (Elahi and Souri, 2006; González-Borrero et al., 2010; Klein et al., 2012; Mowbray and Migani, 2016).

The hysteresis loop for the Fe@CQDs MNCs clearly proved ferromagnetic behavior with a coercive field of around 859 Oe and the value of the saturation magnetization is 20.94 emu/g and was calculated by extrapolating the curve with highest magnetic moment values (Fig. 5). However, the Fe@CQDs MNCs had a retentivity of 15emu/g. The unsaturation in the curve may be due to the some antiferromagnetic character in the Fe@CQDs MNCs. The M-H curve for the Fe/Ag@CQDs BMNCs also showed good hysteresis. The Fe/Ag@CQDs BMNCs however had somewhat less coercivity of order of 587 Oe. The saturation magnetization of Fe/Ag@CQDs BMNCs is 7 emu/g and the retentivity value is 2.7 emu/g. These values are significantly lower in comparison to the parameters obtained for Fe@CQDs MNCs, which is understandable due to the presence of non-ferromagnetic Ag. Thus, these values are still appreciable as the addition of Ag has not destroyed the ferromagnetic nature.

3.2. *Applications*

3.2.1. *Dye degradation*

The degradation of FG dye was studied using Fe NPs, Fe@CQDs MNCs and Fe/Ag@CQDs BMNCs. Fig. 6 (a,b and c) and Fig. 7 (a,b and c) shows the photocatalytic degradation of FG dye using Fe NPs, Fe@CQDs MNCs and Fe/Ag@CQDs BMNCs under two conditions: Set-1: equilibrium adsorption in dark followed by photocatalysis and Set-2: combined adsorptional/photocatalysis directly under sodium light. The FG dye adsorption was studied onto the Fe NPs,

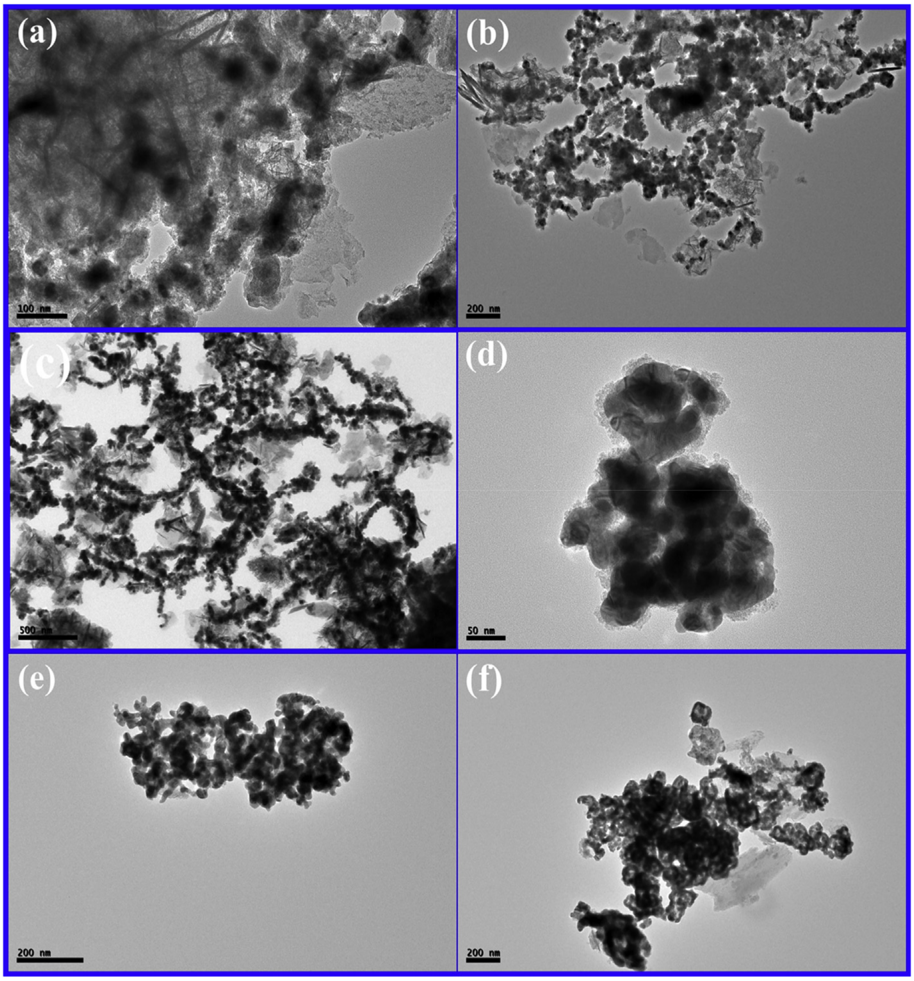

Fig. 3. TEM images of (a, b and c) Fe@CQDs MNCs and (d, e and f) Fe/Ag@CQDs BMNCs.

Fe@CQDs MNCs and Fe/Ag@CQDs BMNCs until adsorption-desorption equilibrium was established by keeping the test sets under dark conditions. Then, the slurries containing dye and Fe NPs, Fe@CQDs MNCs and Fe/Ag@CQDs BMNCs were irradiated with sodium light for further photocatalysis. Under the second set of conditions the FG dye slurries containing Fe NPs, Fe@CQDs MNCs and Fe/Ag@CQDs BMNCs were directly placed in sodium light for combined adsorptional/photocatalysis.

Set-1 (equilibrium adsorption in dark followed by photocatalysis under sodium lamp)

The UV–visible spectral changes of FG dye with reaction time under sodium light in equilibrium adsorption in dark followed by photocatalysis were shown in Fig. 6 (a, b and c). It was observed in set-1, that 12% of FG dye was adsorbed onto Fe NPs in 1 h under dark phase, whereas total 52% of FG dye was degraded by Fe NPs within 4 h of remediation period (Fig. 6d). In case of Fe@CQDs MNCs and Fe/Ag@CQDs BMNCs 17% and 46% of FG dye was adsorbed onto MNCs and BMNCs for 1 h of dark phase and overall 53% and 66% of FG was degraded by Fe@CQDs MNCs and Fe/Ag@CQDs BMNCs (Fig. 6 e and f) (Table 1) (Kansal et al., 2007; Rupa et al., 2007; Vaithiyanathan and Sivakumar, 2011; Valentine Rupa et al., 2011). The photocatalytic degradation mechanism of FG under adsorption followed by photocatalysis condition is described as:

$$\text{Fe NPs/Fe@CQDsMNCs/Fe/Ag@CQDsBMNCs} + \text{fast green} \rightarrow \text{Fe NPs/Fe@CQDsMNCs/Fe/Ag@CQDsBMNCs} - \text{fast greenabsorbed (in dark)} \quad (4)$$

$$\text{Fe NPs/Fe@CQDsMNCs/Fe/Ag@CQDsBMNCs} - \text{fast greenabsorbed} + h\nu \rightarrow \text{Fe NPs/Fe@CQDsMNCs/Fe/Ag@CQDsBMNCs} \left(e^{-} + h^{+}\right) - \text{fast green(in sodium light)} \quad (5)$$

$$\text{OH}^{*} + \text{fast green - Fe NPs/Fe@CQDsMNCs/Fe/Ag@CQDsBMNCs} \rightarrow \text{intermediate product} + \text{degraded product} \quad (6)$$

$$\text{O}_2^{-} + \text{Fast green - Fe NPs/Fe@CQDsMNCs/Fe/Ag@CQDsBMNCs} \rightarrow \text{intermediate product} + \text{degraded product} \quad (7)$$

Set-2 (combined adsorptional/photocatalysis directly under sodium lamp)

The combined adsorptional/photocatalysis of FG dye involves adsorption and photodegradation of dye molecules simultaneously on the surface of Fe NPs, Fe@CQDs MNCs and Fe/Ag@CQDs BMNCs (Barka-Bouaifel et al., 2011; Konstantinou and Albanis, 2004). As the NPs, MNCs and BMNCs contain iron or silver ions these generate electron-hole pairs on irradiation with sodium light which further leads to formation of free radicals. The so generated free radicals

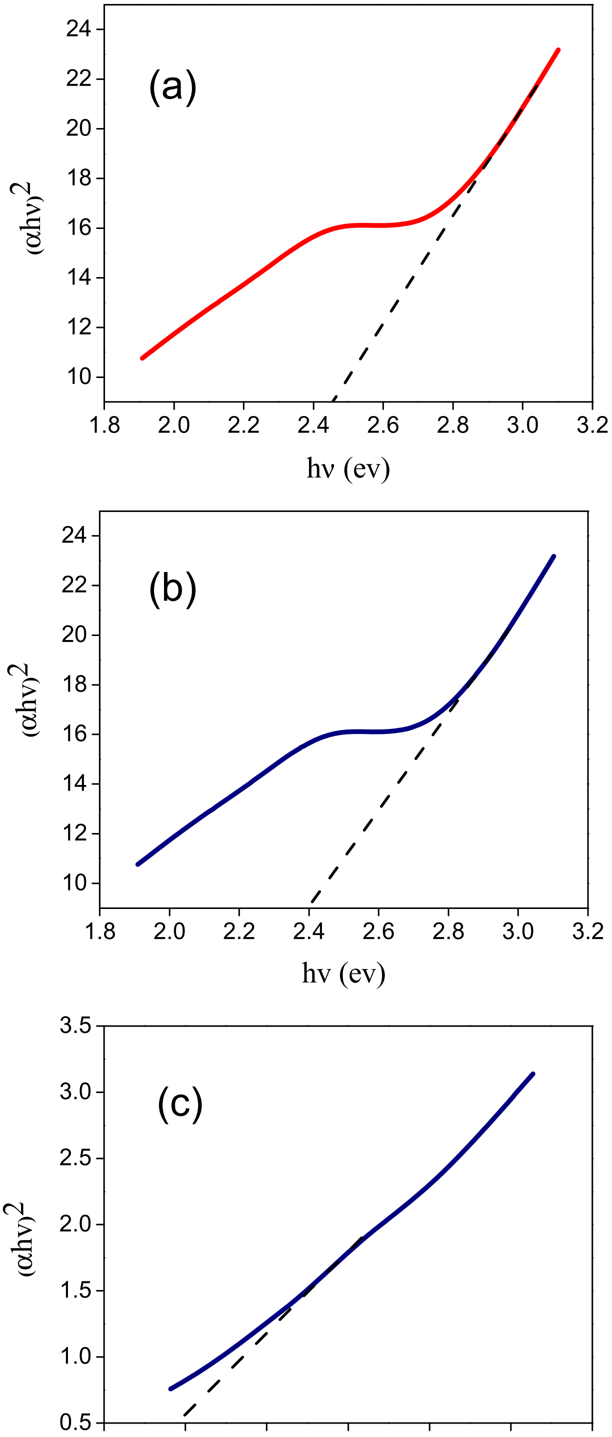

Fig. 4. Band gap of (a) Fe NPs (b) Fe@CQDs MNCs and (c) Fe/Ag@CQDs BMNCs.

disrupt the conjugation in the adsorbed and free dye molecule present in the solution hence, resulting in dye degradation (Loncarevic et al., 2016; Shojaat et al., 2016). The degraded product desorbed from the surface of NPs, MNCs and BMNCs for further adsorption and photocatalysis process. The UV–visible spectral changes of FG dye with reaction time under sodium light in combined adsorptional/photocatalysis were shown in Fig. 7 (a,b and c).

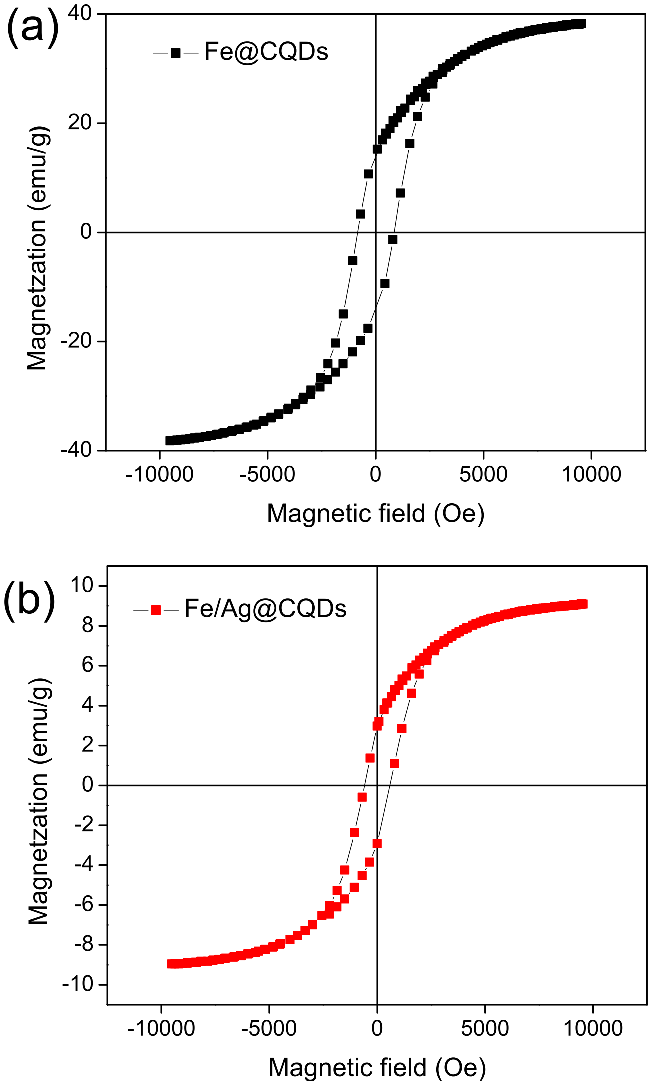

Fig. 5. Hysteresis loop of (a) Fe@CQDs MNCs and (b) Fe/Ag@CQDs BMNCs.

The mechanism for combined adsorptional/photocatalysis degradation of dye is described as follows:

Fe NPs/Fe@CQDsMNCs/Fe/Ag@CQDsBMNCs + fast green → fast green adsorbed (in sodium light) + hv (8)

Fe NPs/Fe@CQDsMNCs/Fe/Ag@CQDsBMNCs (h^+) – fast green + H_2O → Fe NPs/Fe@CQDsMNCs/Fe/Ag@CQDsBMNCs (OH^*) – fast green + H^+ (9)

Fe NPs/Fe@CQDsMNCs/Fe/Ag@CQDsBMNCs (h^+) – fast green absorbed + OH →Fe NPs/Fe@CQDsMNCs/Fe/Ag@CQDsBMNCs (OH^*) – fast green (10)

Fe NPs/Fe@CQDsMNCs/Fe/Ag@CQDsBMNCs (e^-) – fast greenabsorbed + O_2 → Fe NPs/Fe@CQDsMNCs/Fe/Ag@CQDsBMNCs (O_2^{-*}) – fast green (11)

OH^*+ fast green – Fe NPs/Fe@CQDsMNCs/Fe/Ag@CQDsBMNCs → intermediate product → degrade product + free Fe NPs/Fe@CQDsMNCs/Fe/Ag@CQDsBMNCs for reuse (12)

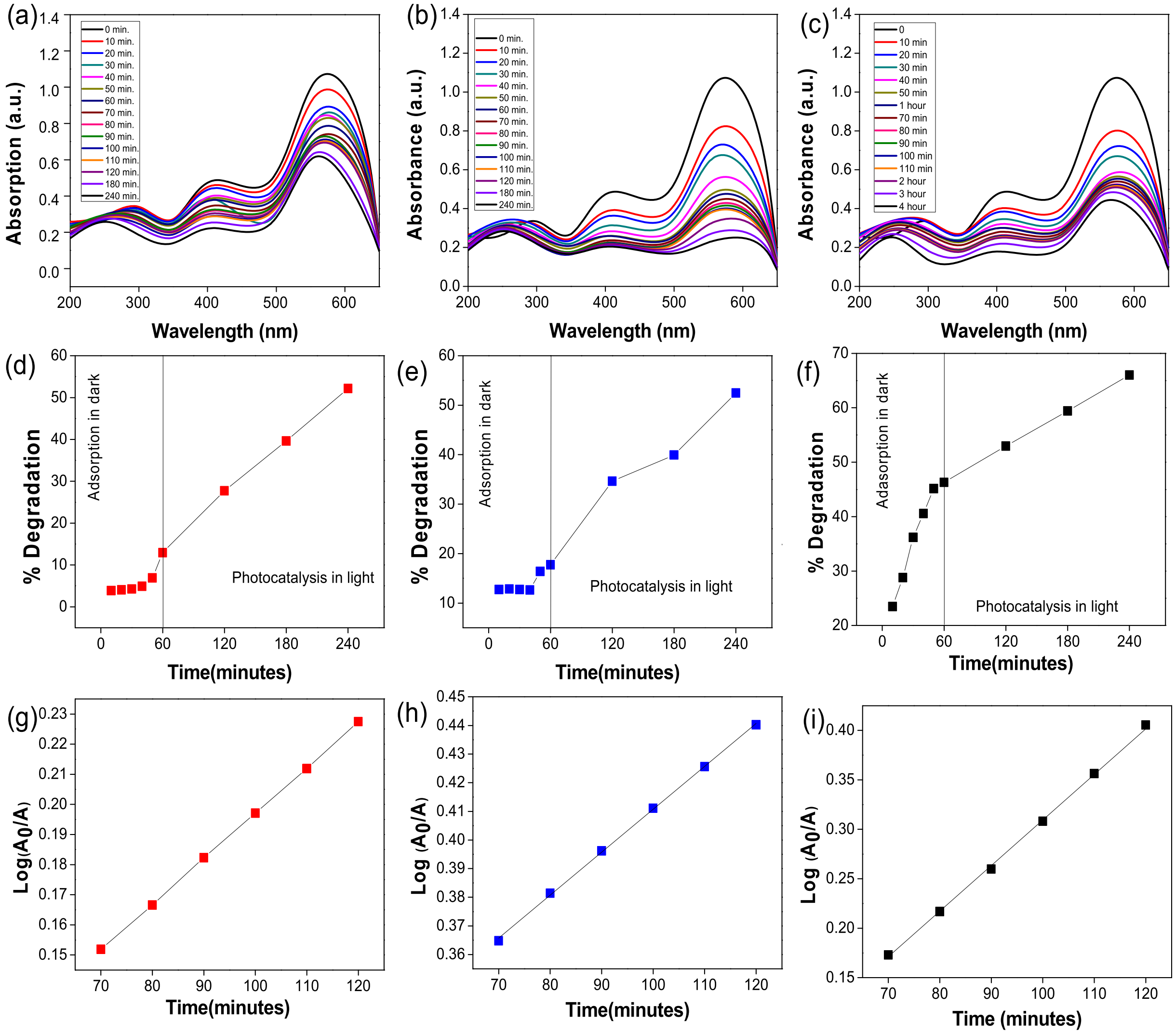

Fig. 6. Spectra of FG: adsorption in dark followed by photocatalysis (Set-1) (a) Fe NPs (b) Fe@CQDs MNCs (c) Fe/Ag@CQDs BMNCs; percentage degradation of FG in presences of (d) Fe NPs (e) Fe@CQDs MNCs (f) Fe/Ag@CQDs BMNCs; pseudo-first-order kinetics for photodegradation of FG (g) Fe NPs (h) Fe@CQDs MNCs (i) Fe/Ag@CQDs BMNCs.

$$O_2^{-*} + \text{fast green} - \text{Fe NPs/Fe@CQDs MNCs/Fe/Ag@CQDsBMNCs} \rightarrow \text{intermediate product} \rightarrow \text{degraded product} + \text{free Fe NPs/Fe@CQDs MNCs/Fe/Ag@CQDsBMNCs for reuse} \quad (13)$$

In combined process, we assume that dye adsorption on to the photocatalyst surface and generation of electron-hole pairs on absorption of light took place at the same time (Sarkar et al., 2016). The adsorption of dye over adsorbent can enable the photodegradation process and increase the degradation rate and ultimately reduce the degradation time. As absorbed dye molecules were more prone to attack of free radicals than the dissolved dye molecules. Thus degradation results were better in this condition. The percent degradation achieved for Fe NPs, Fe@CQDs MNCs and Fe/Ag@CQDs BMNCs in combined adsorptional/photocatalysis condition was 62%, 72% and 74% (Fig. 7 d, e and f). In both sets of condition the kinetics of FG dye degradation fits to linear correlation as shown in Fig. 6 (g, h and i) and Fig. 7 (g, h and i) thus obeys pseudo first-order kinetics. The rate constant and regression coefficients (R^2) value for FG dye degradation are given in Table 2. Based on these values, Fe/Ag@CQDs BMNCs is better photocatalyst then Fe NPs and Fe@CQDs MNCs, proving that bimetallic nanoparticles have superior catalytic behavior than the monometallic nanoparticles.

In the first condition (equilibrium adsorption followed by photocatalysis) possibly the photo catalyst surface gets completely covered by adsorption of dye molecules suppressing further adsorption and thus hindering photodegradation. However, in combined adsorptional/photocatalysis as soon as dye is absorbed onto surface of photocatalyst it gets degraded because of generation of *OH free radicals on absorption of light. Thus degradation is higher and faster in case of second set of reaction condition.

The lower band gap value of Fe/Ag@CQDs BMNCs in comparison to Fe NPs and Fe@CQDs MNCs also reflects that the BMNCs should be better photocatalyst then NPs and MNCs. The comparison of rate constants for combined adsorptional/photocatalysis and adsorption followed photocatalysis (Table 2) clearly indicated that the photocatalysis under combined conditions was more efficient (Pathania et al., 2015a). The decrease in the adsorption band intensities was observed for FG which clearly revealed that the dye was degraded effectively by Fe NPs, Fe@CQDs MNCs and Fe/Ag@CQDs BMNCs.

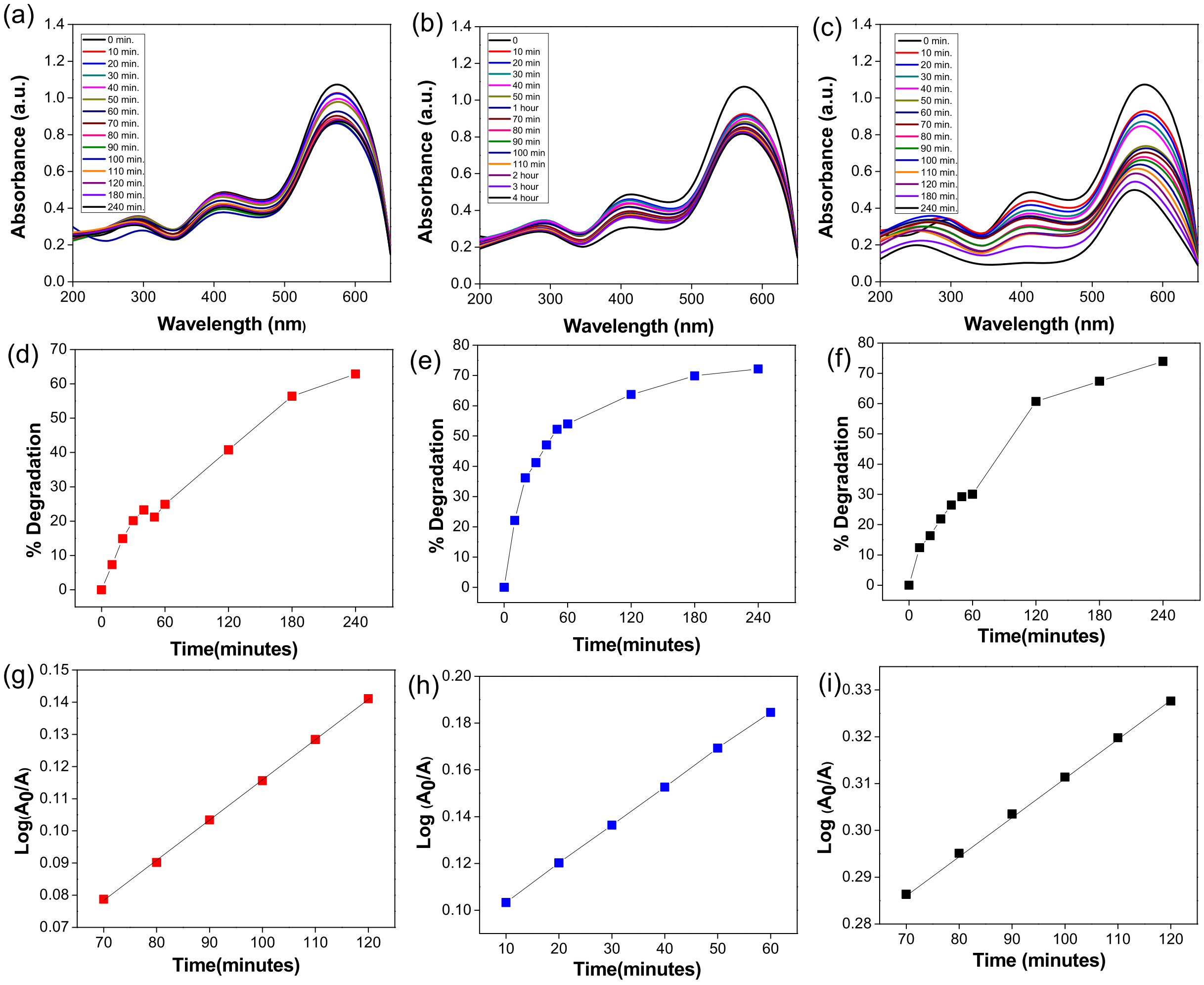

Fig. 7. Spectra of FG: combined adsorptional/photocatalysis (Set-2) (a) Fe NPs (b) Fe@CQDs MNCs (c) Fe/Ag@CQDs BMNCs; percentage degradation of FG in presences of (d) Fe NPs (e) Fe@CQDs MNCs (f) Fe/Ag@CQDs BMNCs; pseudo-first-order kinetics for photodegradation of FG(g) Fe NPs (h) Fe@CQDs MNCs (i) Fe/Ag@CQDs BMNCs.

Table 1
Percent degradation of FG dye using Fe NPs, Fe@CQDs MNCs, Fe/Ag@CQDs BMNCs.

Organic pollutant	NPs/MNCs and BMNCs	Adsorption in dark followed by photocatalysis	Combined adsorptional/photocatalysis
FG Dye	Fe NPs	52%	62%
	Fe@CQDs MNCs	53%	72%
	Fe/Ag@CQDs BMNCs	66%	74%

3.2.1.1. *Oxidation.* In the oxidation of benzyl alcohol, only benzoic acid and benzaldehyde were obtained as reaction products. The percentage yield was slightly high when Fe NPs was used as a catalyst in comparison to that of Fe@CQDs MNCs and Fe/Ag@CQDs BMNCs. The reaction was done at two different temperatures i.e., 80 °C and 100 °C. The reaction was very slow in the absence of the catalyst. The selectivity was high for benzaldehyde on using Fe NPs, and Fe/Ag@CQDs BMNCsin comparison to Fe@CQDs MNCs. It was observed that increase in temperature enhanced the selectivity towards benzoic acid when Fe NPs was used as catalyst. Table 3 shows the percentage yield of benzoic acid and aldehyde at various temperatures. The optimal condition that gave maximum

Table 2
Values of rate constant and regression coefficient for FG degradation using Fe NPs, Fe@CQDs MNCs, Fe/Ag@CQDs BMNCs.

Organic pollutant	Concentration (M)	NPs, MNCs and BMNCs	Adsorption in dark followed by photocatalysis		Combined adsorptional/ photocatalysis	
			$k_{app}(min^{-1})$	R^2	$k_{app}(min^{-1})$	R^2
FG Dye	1×10^{-4}	Fe NPs	0.00465	0.9990	0.00235	0.9984
		Fe@CQD MNCs	0.0015	0.9994	0.00163	0.9997
		Fe/Ag@CQD BMNCs	0.00151	0.9999	0.00125	0.9997

Table 3
Percentage yield of product obtained during oxidation of benzyl alcohol (aldehyde and benzoic acid) at different temperature conditions in absences and presences of Fe NPs, Fe@CQDs MNCs and Fe/Ag @CQDs BMNCs as catalysts.

Materials	Case	Benzyl alcohol:H_2O_2& Temperature (80 or 100 °C)	Acetonitrile (mL)	% Yield	Selectivity %	
					CHO	COOH
Fe NPs	1.	2:1, 80	1	87	62.5	37.5
	2.	2:1, 80	–	80	44	56
	3.	2:1, 100	1	75	43.5	56.5
	4.	2:1, 100	–	80	44	56
Fe@CQDs	1.	2:1, 80	1	75	44.5	55.5
	2.	2:1, 80	–	76	55	45
	3.	2:1, 100	1	78	67	33
	4.	2:1, 100	–	86	47	53
Fe/Ag @CQDs	1.	2:1, 80	1	78	61	39
	2.	2:1, 80	–	80	60	40
	3.	2:1, 100	1	81	59.5	40.5
	4.	2:1, 100	–	86	53	47

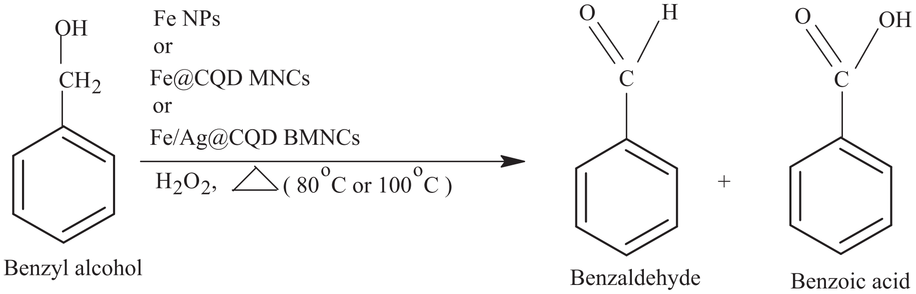

Scheme 1. Oxidation of benzyl alcohol to benzaldehyde and benzoic acid.

yield of 87% (62.5% of benzyl aldehyde and 37.5% benzoic acid) using Fe NPs as catalyst was as follows: amount of catalyst 10 mg, reaction time 2.5 h and acid to alcohol mole ratio 2:1, temperature 80 °C.When Fe@CQDs MNCs was used as catalyst, the conditions that gave maximum yield of 86% (47% benzyl aldehyde and 53% benzoic acid) are as follows: amount of catalyst 10 mg, reaction

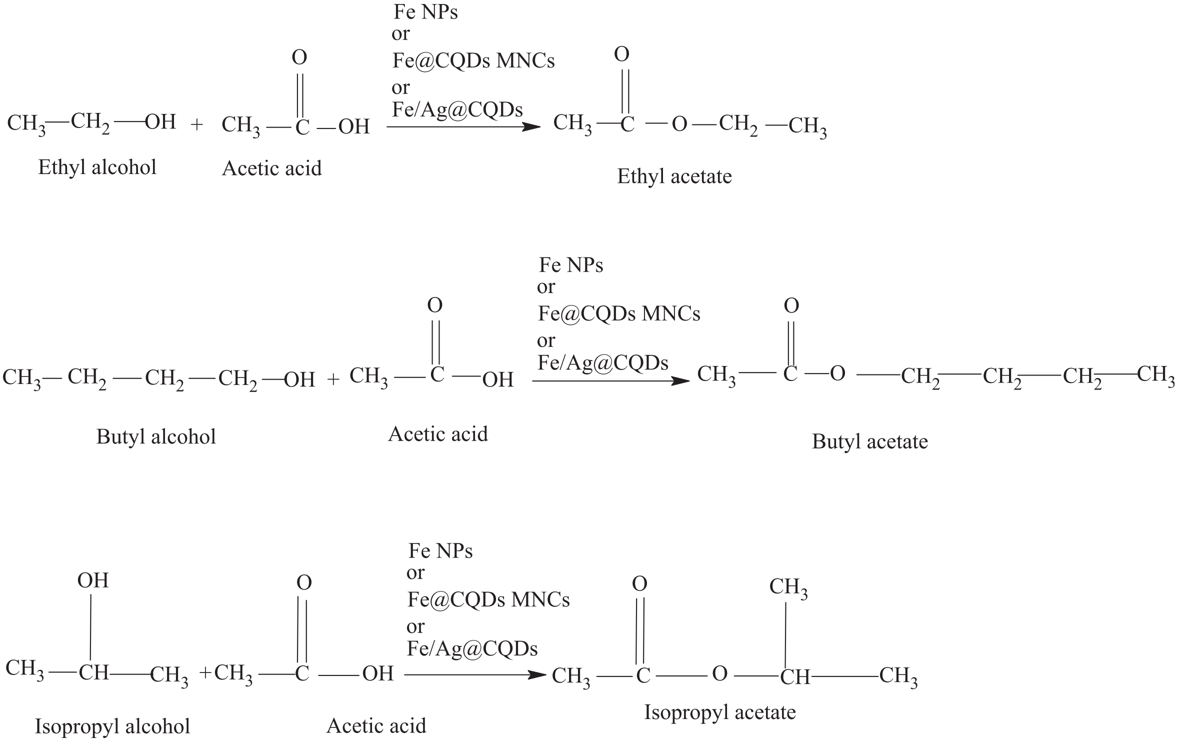

Scheme 2. Esterification reaction of acetic acid with ethyl, isopropyl and butyl alcohol in presences of NPs, MNCs and BMNCs.

Table 4
Percentage yields of different esters obtained using of Fe NPs, Fe@CQDs MNCs and Fe/Ag @CQDs BMNCs as catalysts.

NPs, MNCs and BMNCs used as catalyst	Reaction conditions CH_3COOH:OH (2:1)& Temp. (110 °C) catalyst dosage (10 mg)	Ester	% Yield
Fe NPs	Ethanol	Ethyl acetate	68
	Isopropyl alcohol	Isopropyl acetate	80
	Butonal	Butyl acetate	82
Fe@CQDs	Ethanol	Ethyl acetate	78
	Isopropyl alcohol	Isopropyl acetate	82
	Butonal	Butyl acetate	80
Fe/Ag @CQDs	Ethanol	Ethyl acetate	76
	Isopropyl alcohol	Isopropyl acetate	80
	Butonal	Butyl acetate	84

time 2.5 hand acid to alcohol mole ratio is 2:1, temperature 100 °C. In case of Fe/Ag@CQDs BMNCs, the same reaction conditions resulted in 86% yield (53% benzyl aldehyde and 47% benzoic acidic). Scheme 1 shows the oxidation of benzyl alcohol to

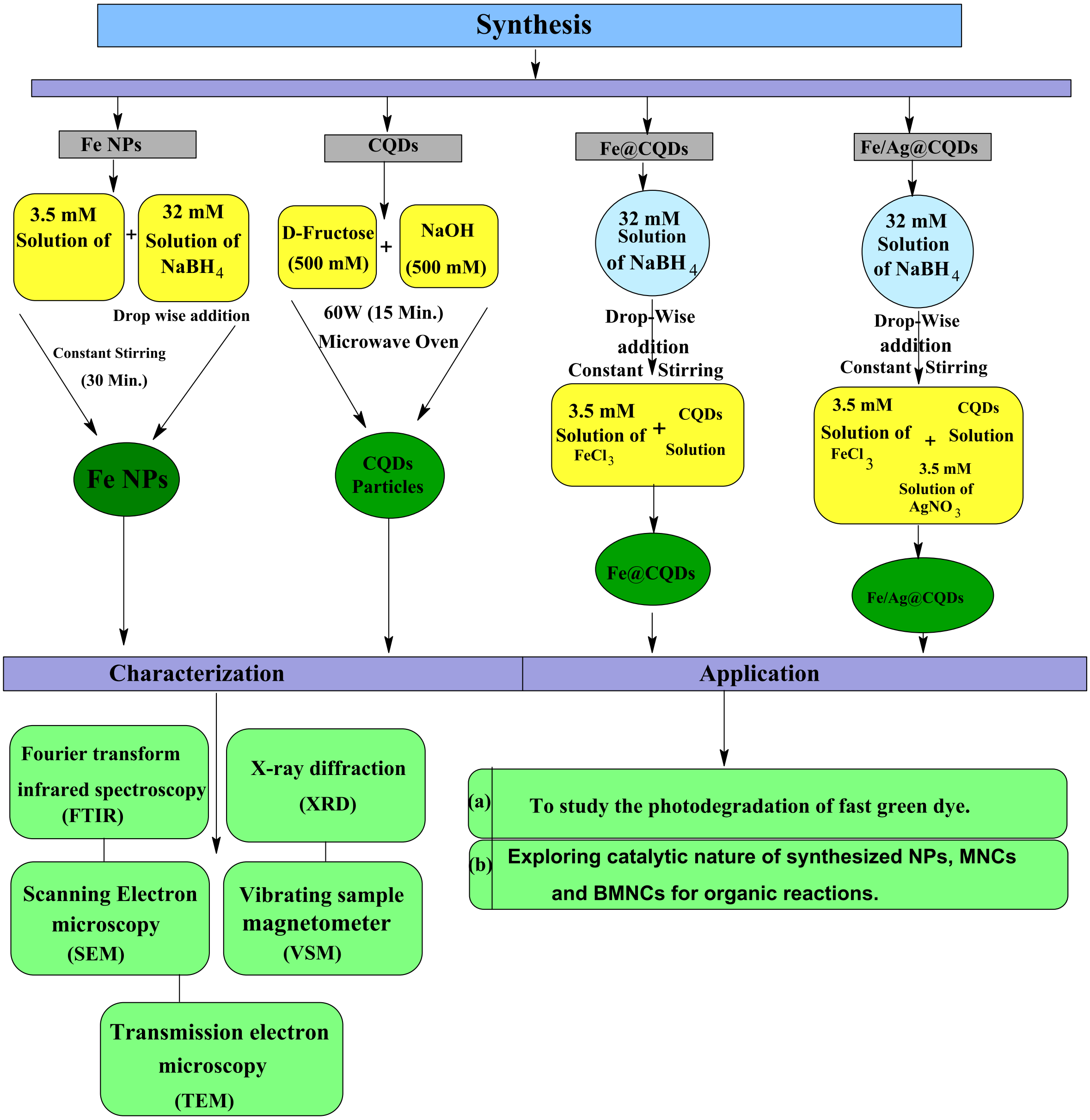

Scheme 3. Flow chart for the synthesis, characterization and application of Fe NPs, CQDs, Fe@CQD MNCs and Fe/Ag@CQD BMNCs.

benzaldehyde and benzoic acid in presences of NPs, MNCs and BMNCs as catalysts.

3.2.1.2. Esterification. Esterification reactions are relatively slow and thus require activation either by a catalyst or by elevated temperature to attain equilibrium conversion to a reasonable degree. Esterification reaction is reversible and equilibrium constant for these reaction are quite low. The byproduct during esterification is water. The presence of water in these reactions leads to hydrolysis hence, results into very low yield. Therefore, cyclohexane was taken as solvent, which removes the water formed during reaction. The conditions that gave maximum yield of ethyl acetate were selected and the same conditions were used for the synthesis of isopropyl acetate and butyl acetate. In comparison to Fe@CQDs MNCs and Fe/Ag@CQDs BMNCs the Fe NPs acted as better catalyst. As reactants achieved equilibrium faster and converted into products, when Fe NPs is used as catalyst. The optimal conditions that gave maximum yield for various acetates were as follows: amount of catalyst 10 mg (Fe NPs than Fe@CQDs MNCs and Fe/Ag@CQDs BMNCs), reaction time 2.5 h and acid to alcohol mole ratio is 2:1. Scheme 2 shows the esterification reaction of acetic acid with ethyl, isopropyl and butyl alcohol in presences of NPs, MNCs and BMNCs as catalysts. Table 4 displays the percentage yields of various esters obtained in the present study. It was observed that butanol gives maximum yield of 82% using Fe NPs as catalyst, isopropyl alcohol gives 82% of maximum yield using Fe@CQDs MNCs as catalyst and butanol give maximum yield of 84% using Fe/Ag@CQDs BMNCs as catalyst. A flow chart for the synthesis, characterization and applications of Fe nanoparticles, monometallic Fe@CQDs MNCs and Fe/Ag@CQDs BMNCs are given in Scheme 3.

4. Conclusion

In the present study, iron based nanoparticles, monometallic and bimetallic nanocomposites were effectively synthesized and characterized. The NPs, MNCs and BMNCs have proven to be potential photocatalyst for the degradation of FG dye in the presences of sodium light under two sets of conditions: equilibrium adsorption in dark followed by photocatalysis and combined adsorptional/photocatalysis directly. The decreases in the adsorption band intensities were observed for FG which clearly revealed that the dye was successfully photodegraded. It was noted that FG degradation was higher in second set of conditions i.e., combined adsorptional/photocatalysis. The catalytic nature of synthesized NPs, MNCs and BMNCs were also explored for oxidation and esterification reactions. It was noticed that in the presence of acetonitrile with ratio 2:1 (BA: H_2O_2) and temperature (80 °C), Fe NPs gave maximum yield of 87%. Thus, it can be concluded that iron based NPs, MNCs, and BMNCs were multifunctional materials with better properties and applications.

Acknowledgements

The authors extend their appreciation to the Deanship of Scientific Research at King Saud University for funding this work through the Research Group No. RG-1436-034. The authors are also thankful to the Shoolini University, Solan, India for providing the lab facilities to carry out the research work. Sultan Qaboos University, Oman is also acknowledged for the characterization of the samples.

Appendix A. Supplementary data

Supplementary data related to this article can be found at https://doi.org/10.1016/j.jclepro.2017.11.122.

References

Akhundi, A., Habibi-Yangjeh, A., 2015. Ternary g-C3N4/ZnO/AgCl nanocomposites: synergistic collaboration on visible-light-driven activity in photodegradation of an organic pollutant. Appl. Surf. Sci. 358, 261–269. https://doi.org/10.1016/j.apsusc.2015.08.149.

Al-Ghouti, M.A., Khraisheh, M.A.M., Allen, S.J., Ahmad, M.N., 2003. The removal of dyes from textile wastewater: a study of the physical characteristics and adsorption mechanisms of diatomaceous earth. J. Environ. Manage 69, 229–238. https://doi.org/10.1016/j.jenvman.2003.09.005.

Barka-Bouaifel, F., Sieber, B., Bezzi, N., Benner, J., Roussel, P., Boussekey, L., Szunerits, S., Boukherroub, R., 2011. Synthesis and photocatalytic activity of iodine-doped ZnO nanoflowers. J. Mater. Chem. 21, 10982–10989.

Bozetine, H., Wang, Q., Barras, A., Li, M., Hadjersi, T., Szunerits, S., Boukherroub, R., 2016. Green chemistry approach for the synthesis of ZnO–carbon dots nanocomposites with good photocatalytic properties under visible light. J. Colloid Interface Sci. 465, 286–294. https://doi.org/10.1016/j.jcis.2015.12.001.

Elahi, M., Souri, D., 2006. Study of optical absorption and optical band gap determination of thin amorphous TeO2 -V2O5 -MoO3 blown films. Indian J. Pure Appl. Phys. 44, 468–472.

Fu, C., Ravindra, N.M., 2012. Magnetic iron oxide nanoparticles: synthesis and applications. Bioinspired Biomim. Nanobiomater. 1, 229–244. https://doi.org/10.1680/bbn.12.00014.

Galán, J., Rodríguez, A., Gómez, J.M., Allen, S.J., Walker, G.M., 2013. Reactive dye adsorption onto a novel mesoporous carbon. Chem. Eng. J. 219, 62–68. https://doi.org/10.1016/j.cej.2012.12.073.

González-Borrero, P.P., Sato, F., Medina, A.N., Baesso, M.L., Bento, A.C., Baldissera, G., Persson, C., Niklasson, G.A., Granqvist, C.G., Ferreira Da Silva, A., 2010. Optical band-gap determination of nanostructured WO3 film. Appl. Phys. Lett. 96, 10–13. https://doi.org/10.1063/1.3313945.

Gorham, J.M., MacCuspie, R.I., Klein, K.L., Fairbrother, D.H., Holbrook, D., 2012. UV-induced photochemical transformations of citrate-capped silver nanoparticle suspensions. J. Nanoparticle Res. 14, 1139–1154. https://doi.org/10.1007/s11051-012-1139-3.

Gupta, A.K., Gupta, M., 2005. Synthesis and surface engineering of iron oxide nanoparticles for biomedical applications. Biomaterials 26, 3995–4021. https://doi.org/10.1016/j.biomaterials.2004.10.012.

He, X., Qi, W., 2002. A novel approach to prepare conductive polyaninine/nanocrystal- line TiO2 composites. Chem. Mater. 14, 2158–2165.

Herranz, F., Salinas, B., Groult, H., Pellico, J., Lechuga-Vieco, A.V., Bhavesh, R., Ruiz-Cabello, J., 2014. Superparamagnetic nanoparticles for atherosclerosis imaging. Nanomaterials 4, 408–438. https://doi.org/10.3390/nano4020408.

Kansal, S.K., Singh, M., Sud, D., 2007. Studies on photodegradation of two commercial dyes in aqueous phase using different photocatalysts. J. Hazard. Mater. 141, 581–590. https://doi.org/10.1016/j.jhazmat.2006.07.035.

Klein, P.B., Nwagwu, U., Edgar, J.H., Freitas, J.A., 2012. Photoluminescence investigation of the indirect band gap and shallow impurities in icosahedral B 12As 2. J. Appl. Phys. 112 https://doi.org/10.1063/1.4729920, 0135081–01350812.

Konstantinou, I.K., Albanis, T.A., 2004. TiO2-assisted photocatalytic degradation of azo dyes in aqueous solution: kinetic and mechanistic investigations: a review. Appl. Catal. B Environ. 49, 1–14. https://doi.org/10.1016/j.apcatb.2003.11.010.

Kumar, A., Sharma, G., Naushad, M., Thakur, S., 2015. SPION/β-cyclodextrin core-shell nanostructures for oil spill remediation and organic pollutant removal from waste water. Chem. Eng. J. 280, 175–187. https://doi.org/10.1016/j.cej.2015.05.126.

Kumar, A., Naushad, M., Rana, A., Inamuddin, Preeti, Sharma, G., Ghfar, A.A., Stadler, F.J., Khan, M.R., 2017a. ZnSe-WO 3 nano-hetero-assembly stacked on Gum ghatti for photo-degradative removal of Bisphenol A: symbiose of adsorption and photocatalysis. Int. J. Biol. Macromol. 104, 1172–1184. https://doi.org/10.1016/j.ijbiomac.2017.06.116.

Kumar, A., Shalini Sharma, G., Naushad, M., Kumar, A., Kalia, S., Guo, C., Mola, G.T., 2017b. Facile hetero-assembly of superparamagnetic Fe3O4/BiVO4 stacked on biochar for solar photo-degradation of methyl paraben and pesticide removal from soil. J. Photochem. Photobiol. A Chem. 337, 118–131. https://doi.org/10.1016/j.jphotochem.2017.01.010.

Loncarevic, D., Dostanic, J., Radonjic, V., Ivkovic, Lj.Z., Jovanović, D.M., 2016. Simultaneous photodegradation of two textile dyes using TiO2 as a catalyst. React. Kinet. Mech. Catal. 118, 153–164. https://doi.org/10.1007/s11144-016-0990-0.

Martinez-Cabanas, M., Lopez-Garcia, M., Barriada, J.L., Herrero, R., Sastre de Vicente, M.E., 2016. Green synthesis of iron oxide nanoparticles. Development of magnetic hybrid materials for efficient As(V) removal. Chem. Eng. J. 301, 83–91. https://doi.org/10.1016/j.cej.2016.04.149.

Martínez-Mera, I., Espinosa-Pesqueira, M.E., Pérez-Hernández, R., Arenas-Alatorre, J., 2007. Synthesis of magnetite (Fe3O4) nanoparticles without surfactants at room temperature. Mater. Lett. 61, 4447–4451. https://doi.org/10.1016/j.matlet.2007.02.018.

Millo, O., Katz, D., Cao, Y., Banin, U., 2001. Imaging and spectroscopy of artificial-atom states in core/shell nanocrystal quantum dots. Phys. Rev. Lett. 86, 5751–5754. https://doi.org/10.1103/PhysRevLett.86.5751.

Mittal, A., Naushad, M., Sharma, G., Alothman, Z.A., Wabaidur, S.M., Alam, M., 2016. Fabrication of MWCNTs/ThO2 nanocomposite and its adsorption behavior for the removal of Pb(II) metal from aqueous medium. Desalin. Water Treat. 57, 21863–21869. https://doi.org/10.1080/19443994.2015.1125805.

Mostafaei, A., Nasirpouri, F., 2013. Preparation and characterization of a novel conducting nanocomposite blended with epoxy coating for antifouling and antibacterial applications. J. Coatings Technol. Res. 10, 679–694. https://doi.org/10.1007/s11998-013-9487-1.

Mowbray, D.J., Migani, A., 2016. Optical absorption spectra and excitons of dye-substrate interfaces: catechol on TiO2(110). J. Chem. Theory Comput. 12, 2843–2852. https://doi.org/10.1021/acs.jctc.6b00217.

Naushad, M., Vasudevan, S., Sharma, G., Kumar, A., ALOthman, Z.A., 2015. Adsorption kinetics, isotherms, and thermodynamic studies for Hg2+ adsorption from aqueous medium using alizarin red-S-loaded amberlite IRA-400 resin. Desalin. Water Treat. 3994, 2237–2245. https://doi.org/10.1080/19443994.2015.1090914.

Naushad, M., Ahamad, T., Sharma, G., Al-Muhtaseb, A.H., Albadarin, A.B., Alam, M.M., ALOthman, Z.A., Alshehri, S.M., Ghfar, A.A., 2016. Synthesis and characterization of a new starch/SnO2 nanocomposite for efficient adsorption of toxic Hg2+ metal ion. Chem. Eng. J. 300, 306–316. https://doi.org/10.1016/j.cej.2016.04.084.

Omidi, A., Habibi-Yangjeh, A., Pirhashemi, M., 2013. Application of ultrasonic irradiation method for preparation of ZnO nanostructures doped with Sb+3 ions as a highly efficient photocatalyst. Appl. Surf. Sci. 276, 468–475. https://doi.org/10.1016/j.apsusc.2013.03.118.

Pathania, D., Sharma, G., Kumar, A., Naushad, M., Kalia, S., Sharma, A., Alothman, Z.A., 2015a. Combined sorptional–photocatalytic remediation of dyes by polyaniline Zr(IV) selenotungstophosphate nanocomposite. Toxicol. Environ. Chem. 97, 526–537.

Pathania, D., Gupta, D., Al-Muhtaseb, A.H., Sharma, G., Kumar, A., Naushad, M., Ahamad, T., Alshehri, S.M., 2016a. Photocatalytic degradation of highly toxic dyes using chitosan-g-poly(acrylamide)/ZnS in presence of solar irradiation. J. Photochem. Photobiol. A Chem. 329, 61–68. https://doi.org/10.1016/j.jphotochem.2016.06.019.

Pathania, D., Katwal, R., Sharma, G., Naushad, M., Khan, M.R., Al-Muhtaseb, A.H., 2016b. Novel guar gum/Al2O3 nanocomposite as an effective photocatalyst for the degradation of malachite green dye. Int. J. Biol. Macromol. 87, 366–374. https://doi.org/10.1016/j.ijbiomac.2016.02.073.

Poormohammadi-Ahandani, Z., Habibi-Yangjeh, A., 2010. Fast, green and template-free method for preparation of Zn1−xCdxS nanoparticles using microwave irradiation and their photocatalytic activities. Phys. E Low Dimensional Syst. Nanostructures 43, 216–223. https://doi.org/10.1016/j.physe.2010.07.009.

Rai, M.K., Deshmukh, S.D., Ingle, A.P., Gade, A.K., 2012. Silver nanoparticles: the powerful nanoweapon against multidrug-resistant bacteria. J. Appl. Microbiol. 112, 841–852. https://doi.org/10.1111/j.1365-2672.2012.05253.x.

Rupa, A.V., Manikandan, D., Divakar, D., Sivakumar, T., 2007. Effect of deposition of Ag on TiO2 nanoparticles on the photodegradation of reactive Yellow-17. J. Hazard. Mater. 147, 906–913. https://doi.org/10.1016/j.jhazmat.2007.01.107.

Sarkar, A.K., Saha, A., Tarafder, A., Panda, A.B., Pal, S., 2016. Efficient removal of toxic dyes via simultaneous adsorption and solar light driven photodegradation using recyclable functionalized amylopectin-TiO2-Au nanocomposite. ACS Sustain. Chem. Eng. 4, 1679–1688. https://doi.org/10.1021/acssuschemeng.5b01614.

Sharma, G., Naushad, M., Kumar, A., Devi, S., Khan, M.R., 2015. Lanthanum/Cadmium/Polyaniline bimetallic nanocomposite for the photodegradation of organic pollutant. Iran. Polym. J. 25, 1003–1013. https://doi.org/10.1007/s13726-015-0388-2.

Sharma, G., Gupta, V.K., Agarwal, S., Kumar, A., Thakur, S., Pathania, D., 2016a. Fabrication and characterization of Fe@MoPO nanoparticles: ion exchange behavior and photocatalytic activity against malachite green. J. Mol. Liq. 219, 1137–1143. https://doi.org/10.1016/j.molliq.2016.04.046.

Sharma, G., Kumar, A., Naushad, M., Pathania, D., Sillanpaa, M., 2016b. Polyacrylamide@Zr(IV)vanadophosphate nanocomposite: ion exchange properties, antibacterial activity, and photocatalytic behavior. J. Ind. Eng. Chem. 33, 201–208. https://doi.org/10.1016/j.jiec.2015.10.011.

Sharma, G., Naushad, M., Pathania, D., Kumar, A., 2016c. A multifunctional nanocomposite pectin thorium(IV) tungstomolybdate for heavy metal separation and photoremediation of malachite green. Desalin. Water Treat. 57, 19443–19455. https://doi.org/10.1080/19443994.2015.1096834.

Sharma, G., Kumar, A., Sharma, S., Naushad, M., Prakash Dwivedi, R., ALOthman, Z.A., Mola, G.T., 2017. Novel development of nanoparticles to bimetallic nanoparticles and their composites: a review. J. King Saud. Univ. Sci. https://doi.org/10.1016/j.jksus.2017.06.012.

Sharma, G., Alothman, Z.A., Kumar, A., Sharma, S., Ponnusamy, S.K., Naushad, M., 2017a. Fabrication and characterization of a nanocomposite hydrogel for combined photocatalytic degradation of a mixture of malachite green and fast green dye. J. Nanotechnol. Environ. Eng 2, 1–4.

Sharma, G., Kumar, D., Kumar, A., Al-Muhtaseb, A.H., Pathania, D., Naushad, M., Mola, G.T., 2017b. Revolution from monometallic to trimetallic nanoparticle composites, various synthesis methods and their applications: a review. Mater. Sci. Eng. C 71, 1216–1230. https://doi.org/10.1016/j.msec.2016.11.002.

Sharma, G., Naushad, M., Kumar, A., Rana, S., Sharma, S., Bhatnagar, A., Stadler, F.J., Ghfar, A.A., Khan, M.R., 2017c. Efficient removal of coomassie brilliant blue R-250 dye using starch/poly(alginic acid-cl-acrylamide) nanohydrogel. Process Saf. Environ. Prot. 109, 301–310. https://doi.org/10.1016/j.psep.2017.04.011.

Shojaat, R., Saadatjoo, N., Karimi, A., Aber, S., 2016. Simultaneous adsorption-degradation of organic dyes using MnFe2O4/calcium alginate nanocomposites coupled with GOx and laccase. J. Environ. Chem. Eng. 4, 1722–1730. https://doi.org/10.1016/j.jece.2016.02.029.

Sun, S.H., Zeng, H., 2002. Size-controlled synthesis of magnetite nanoparticles. J. Am. Chem. Soc. 124, 8204–8205. https://doi.org/10.1021/ja026501x.

Tang, H., Lu, A., Li, L., Zhou, W., Xie, Z., Zhang, L., 2013. Highly antibacterial materials constructed from silver molybdate nanoparticles immobilized in chitin matrix. Chem. Eng. J. 234, 124–131. https://doi.org/10.1016/j.cej.2013.08.096.

Vaithiyanathan, R., Sivakumar, T., 2011. Studies on photocatalytic activity of the synthesised TiO 2 and Ag/TiO 2 photocatalysts under UV and sunlight irradiations. Water Sci. Technol. 63, 377–384. https://doi.org/10.2166/wst.2011.231.

Valentine Rupa, A., Vaithiyanathan, R., Sivakumar, T., 2011. Noble metal modified titania catalysts in the degradation of Reactive Black 5: a kinetic approach. Water Sci. Technol. 64, 1040–1045. https://doi.org/10.2166/wst.2011.524.

Wang, Y., Zhao, H., Zhao, G., 2015. Iron-copper bimetallic nanoparticles embedded within ordered mesoporous carbon as effective and stable heterogeneous Fenton catalyst for the degradation of organic contaminants. Appl. Catal. B Environ. 164, 396–406. https://doi.org/10.1016/j.apcatb.2014.09.047.

Yang, X.H., Fu, H.T., Wang, X.C., Yang, J.L., Jiang, X.C., Yu, A.B., 2014. Synthesis of silver-titanium dioxide nanocomposites for antimicrobial applications. J. Nanoparticle Res. 16 https://doi.org/10.1007/s11051-014-2526-8.

Yu, Y., Zhao, Y., Huang, T., Liu, H., 2009. Shape-controlled synthesis of palladium nanocrystals by microwave irradiation. Pure Appl. Chem. 81, 2377–2385. https://doi.org/10.1351/PAC-CON-08-11-22.

Zhang, J., Zhang, L., Zhou, S., Chen, H., Zhong, H., Zhao, Y., Wang, X., 2014. Magnetically separable attapulgite-TiO2-FexOy composites with superior activity towards photodegradation of methyl orange under visible light radiation. J. Ind. Eng. Chem. 20, 3884–3889. https://doi.org/10.1016/j.jiec.2013.12.094.

Zhang, L., Liu, Z., Wang, Y., Xie, R., Ju, X.J., Wang, W., Lin, L.G., Chu, L.Y., 2017. Facile immobilization of Ag nanoparticles on microchannel walls in microreactors for catalytic applications. Chem. Eng. J. 309, 691–699. https://doi.org/10.1016/j.cej.2016.10.038.

List of abbreviation

NPs: Nanoparticles
Fe: Iron
Ag: Silver
FG: Fast green
CQDs: Carbon quantum dots
VSM: Vibrating sample magnetometer
FTIR: Fourier transform infra-red
C_0: Initial concentration
C_P: Final concentration
W_R: Initial weight of reactant
W_P: Initial weight of product
Fe@CQDs: Iron@Carbon quantum dots
Fe/Ag@CQDs: Iron/silver@Carbon quantum dots
SEM: Scanning electron microscopy
MNCs: Monometallic nanocomposite
BMNCs: Bimetallic nanocomposite
TEM: Transmission electron microscopy
XRD: X-Ray diffraction
VSM: Vibrating sample magnetometer